WAVES IN SPATIALLY-DISORDERED NEURAL FIELDS: A CASE STUDY IN UNCERTAINTY QUANTIFICATION

CARLO R. LAING

Abstract. Neural field models have been used for many years to model a variety of macroscopic spatiotemporal patterns in the cortex. Most authors have considered homogeneous domains, resulting in equations that are translationally invariant. However, there is an obvious need to better understand the dynamics of such neural field models on heterogeneous domains. One way to include heterogeneity is through the introduction of randomly-chosen "frozen" spatial noise to the system. In this chapter we investigate the effects of including such noise on the speed of a moving "bump" of activity in a particular neural field model. The spatial noise is parameterised by a large but finite number of random variables, and the effects of including it can be determined in a computationally-efficient way using ideas from the field of Uncertainty Quantification. To determine the average speed of a bump in this type of heterogeneous domain involves evaluating a high-dimensional integral, and a variety of methods are compared for doing this. We find that including heterogeneity of this form in a variety of ways always slows down the moving bump.

1. Introduction

Neural field models have been used for many years as models of large-scale pattern formation in the cortex [9, 13, 1, 32, 33, 35, 16, 28]. These models are typically formulated as nonlocal partial differential equations in space and time where the nonlocality arises via spatial integrals, meant to represent the influence of neurons at many different spatial locations on the dynamics at a specific location [13, 9]. They have been used to model a variety of neurophysiological phenomena such as working memory [33], orientation tuning in the visual cortex [4] and EEG rhythms [39]. Much of the analysis of patterns in these models has assumed that the domain is homogeneous and thus the governing equations are translationally invariant. This invariance allows one to, for example, choose the origin of space to simplify analysis. When studying travelling waves, this invariance means that it is relatively easy to construct "bumps" and fronts of activity which move with a constant speed. However, the brain is far from homogeneous and it is of interest to understand how various forms of heterogeneity affect the properties of moving waves in neural field models.

A number of authors have considered including heterogeneity in neural field models by introducing spatially periodic modulation of various components of the model such as connectivity [7, 25] and input currents [14]. This type of heterogeneity is structured rather than random, but a number of other authors have considered the effects of truly random hetereogeneity, in either space, time, or both. For example, the authors [5] considered the effects on the speed of a front of a spatially uniform firing rate threshold which randomly fluctuated in time. They found that such fluctuations always increased the average front speed. Coombes et al. [15] briefly considered a variety of forms of

Date: May 5, 2014.

Key words and phrases. neural field, uncertainty quantification, pattern formation, heterogeneity, integration.

heterogeneity such as adding "frozen" spatial noise, and driving the system with temporal noise. Bressloff [8] adapted ideas from PDE theory to study the effects of slowly modulated (in space) synaptic connectivity on the invasion and extinction of activity in a neural field model. Several authors have very recently considered the effects of additive spatio-temporal noise on the dynamics of a neural field [11, 26, 24, 6].

In this chapter we will use ideas from the relatively new field of Uncertainty Quantification (UQ) to investigate the effects of spatial heterogeneity on the dynamics of moving "bumps" in a particular neural field model. Traditionally, numerical models of physical phenomena have been solved under the assumption that both the initial conditions and all values of relevant parameters are known exactly. However, recent increases in computational power have meant that it is now possible to solve a model where one or more parameters are not known exactly, but are known (or assumed) to come from some distribution(s). For our purposes, UQ involves a systematic investigation of the effects of this uncertainty in parameter values on quantities of interest. The field of UQ is large and rapidly growing [34, 45, 42] and here we will only use those aspects of it which are directly relevant.

2. Model and Analysis

The model we first consider is governed by the following equations:

$$\frac{\partial u(x,t)}{\partial t} = -u(x,t) + \int_0^{2\pi} G(x-y)F[u(y,t) - a(y,t) + h(y)]dy \tag{1}$$

$$\tau\frac{\partial a(x,t)}{\partial t} = Bu(x,t) - a(x,t) \tag{2}$$

where $u(x,t)$ represents the average voltage of neurons at position $x \in [0, 2\pi]$ at time t, and $a(x,t)$ represents the value of a slow variable at x and t which provides negative feedback to the dynamics of u. Similar models have been studied elsewhere [36, 15, 10, 31, 30]. Periodic boundary conditions are used, B and τ are positive constants, and the firing rate function is given by

$$F[u] = \frac{1}{1+e^{-20(u-0.4)}} \tag{3}$$

Note that F is bounded between 0 and 1 and is an increasing function. The function $h(y)$, to be specified below, provides the spatial heterogeneity to the system. We choose the coupling function to be $G(x) = 0.09 + 0.45\cos x$; note that this is even. The physical interpretation of the model is that neurons with average voltage u fire at a frequency $F[u]$, and the strength of connections between neurons at position x and those at position y is $G(x-y)$. Summing (integrating) over all y gives the nonlinear term in (1), and this is the influence of all other neurons on those at position x. The variable a is driven up when u is high and down when u is low, with a time-scale of τ. The way that a appears in (1) means that it acts a negative feedback mechanism.

For suitable choices of parameters the system (1)-(2) is capable of supporting travelling "bumps" of activity. See Fig. 1(a). A bump is defined to be a state in which one region of the domain is active, i.e. has $F[u] \approx 1$, while the rest of the domain is inactive, i.e. has $F[u] \approx 0$. When $h(y)$ is constant the bumps travel with constant speed and profile, while if $h(y)$ is not constant — but is sufficiently small — bumps continue to travel, but with non-constant speed and profile. See Fig. 1(b)-(d). Because the domain has periodic boundary conditions, these modulated bumps are periodic in time. Our goal is the determine, in a computationally-efficient manner, the expected effects of making $h(y)$ a

random function of y, in a way to be explained below. In particular we wish to answer the question: given that $h(y)$ is randomly chosen from some distribution of functions, what is the expected value of the average speed of the resulting travelling bump (after transients have decayed)? As mentioned, we will answer this using techniques from the field of uncertainty quantification [34, 41]. Here, the uncertainty arises because we do not exactly know $h(y)$. This uncertainty then affects the dynamics of the neural field model, making measurable quantities such as the bump speed uncertain, i.e. have some distribution of values. Typically, we would like to describe this distribution so that we can calculate, for example, its mean.

The form of the coupling function $G(x)$ allows us to write (1) as

$$\begin{aligned}\frac{\partial u(x,t)}{\partial t} &= -u(x,t) + 0.09\int_0^{2\pi} F[u(y,t)-a(y,t)+h(y)]\ dy \\ &\quad + 0.45\cos x\int_0^{2\pi} F[u(y,t)-a(y,t)+h(y)]\cos y\ dy \\ &\quad + 0.45\sin x\int_0^{2\pi} F[u(y,t)-a(y,t)+h(y)]\sin y\ dy\end{aligned} \tag{4}$$

As noted [31], if we expand $u(x,t)$ and $a(x,t)$ in Fourier series in x we see that terms of the form $\sin(nx)$ and $\cos(nx)$ for $n > 1$ will decay to zero, and since we are not interested in transients we write

$$u(x,t) = u^0(t) + u^c(t)\cos x + u^s(t)\sin x \tag{5}$$

and

$$a(x,t) = a^0(t) + a^c(t)\cos x + a^s(t)\sin x \tag{6}$$

Substituting these expansions into (2) and (4) we find that the modulated bumps of interest are described by the six ordinary differential equations (ODEs)

$$\frac{du^0}{dt} = -u^0 + 0.09\int_0^{2\pi} F[u^0 - a^0 + (u^c-a^c)\cos x + (u^s-a^s)\sin x + h(x)]\ dx \tag{7}$$

$$\frac{du^c}{dt} = -u^c + 0.45\int_0^{2\pi} F[u^0 - a^0 + (u^c-a^c)\cos x + (u^s-a^s)\sin x + h(x)]\cos x\ dx \tag{8}$$

$$\frac{du^s}{dt} = -u^s + 0.45\int_0^{2\pi} F[u^0 - a^0 + (u^c-a^c)\cos x + (u^s-a^s)\sin x + h(x)]\sin x\ dx \tag{9}$$

$$\tau\frac{da^0}{dt} = Bu^0 - a^0 \tag{10}$$

$$\tau\frac{da^c}{dt} = Bu^c - a^c \tag{11}$$

$$\tau\frac{da^s}{dt} = Bu^s - a^s \tag{12}$$

We note that the number of ODEs above (six) is an immediate consequence of using only a constant and $\cos x$ term in the coupling function $G(x)$. Our coupling function can be thought of as the truncation of the Fourier series of a general 2π-periodic function.

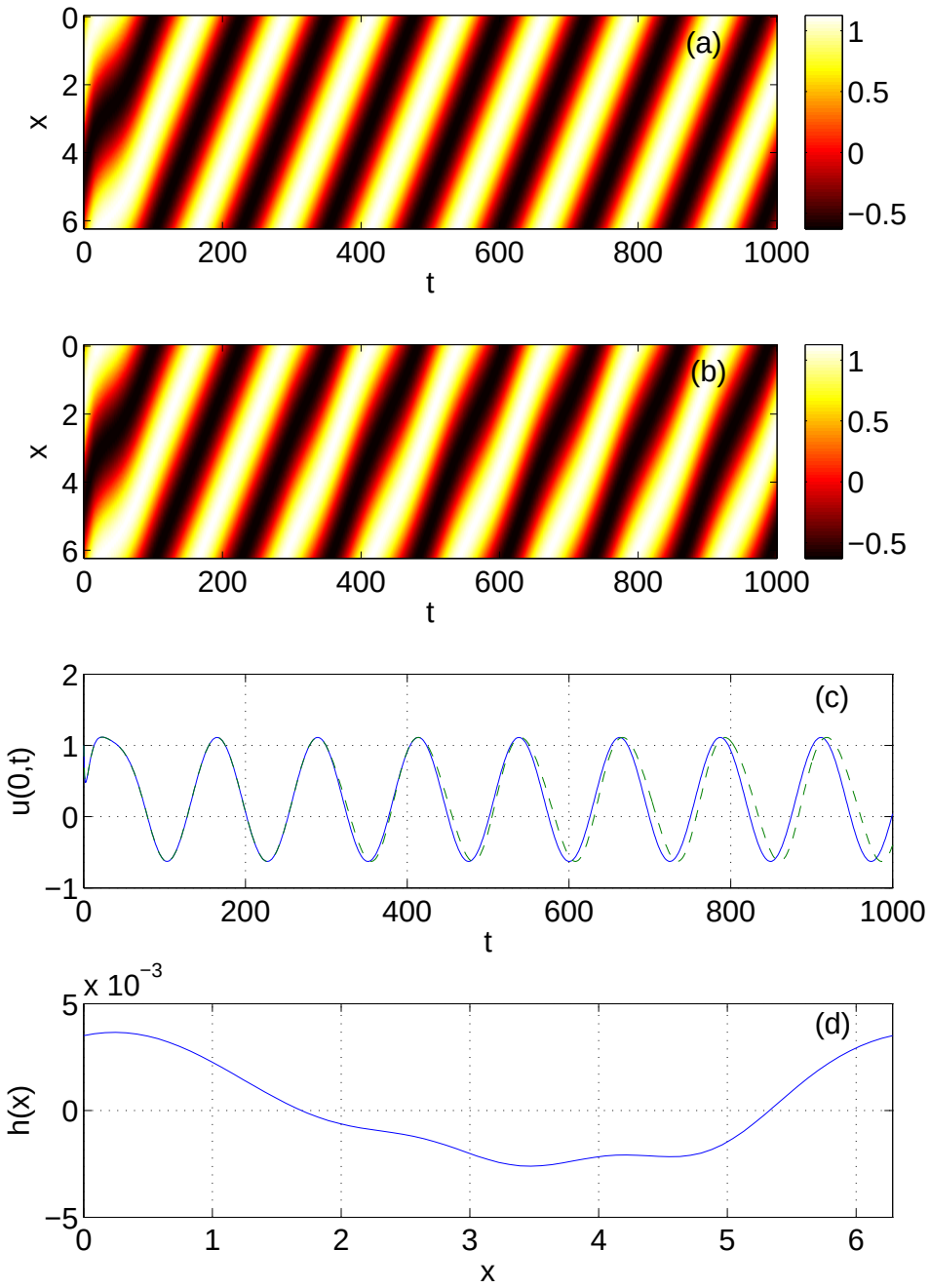

FIGURE 1. Travelling bumps of activity in the model (1)-(2) when (a): $h(x) = 0$ and (b): when $h(x)$ is as shown in (d) for $t > 300$, $h(x) = 0$ for $t < 300$. Panel (c) shows $u(0,t)$ for the solution in panel (a) (blue solid line) and the solution in panel (b) (green dashed line). We see that non-zero $h(x)$ slightly slows the bump. Parameters: $B = 0.1, \tau = 14$.

Including more terms in this truncation would lead to the system being described by more ODEs, in the obvious way: each new harmonic would result in 4 more ODEs.

For a given $h(x)$ we can find the average speed of the resulting bump by finding the relevant periodic solution of (7)-(12). The average speed is then 2π (the size of the domain) divided by the period of this orbit. However, numerically integrating (7)-(12)

is computationally costly, and since we are only interested in periodic solutions of these ODEs we represent their solutions as truncated Fourier series in time, i.e. we write

$$u^0(t) = u_0^0 + \sum_{i=1}^{M} \left[u_i^0 \cos(i\omega t) + u_{M+i}^0 \sin(i\omega t)\right] \tag{13}$$

$$u^c(t) = u_0^c + \sum_{i=1}^{M} \left[u_i^c \cos(i\omega t) + u_{M+i}^c \sin(i\omega t)\right] \tag{14}$$

$$u^s(t) = u_0^s + \sum_{i=1}^{M} \left[u_i^s \cos(i\omega t) + u_{M+i}^s \sin(i\omega t)\right] \tag{15}$$

$$a^0(t) = a_0^0 + \sum_{i=1}^{M} \left[a_i^0 \cos(i\omega t) + a_{M+i}^0 \sin(i\omega t)\right] \tag{16}$$

$$a^c(t) = a_0^c + \sum_{i=1}^{M} \left[a_i^c \cos(i\omega t) + a_{M+i}^c \sin(i\omega t)\right] \tag{17}$$

$$a^s(t) = a_0^s + \sum_{i=1}^{M} \left[a_i^s \cos(i\omega t) + a_{M+i}^s \sin(i\omega t)\right] \tag{18}$$

where $\omega = 2\pi/T$ and T is the unknown period of the periodic orbit we wish to find. We have

$$\frac{du^0}{dt} = \sum_{i=1}^{M} \left[-i\omega u_i^0 \sin(i\omega t) + i\omega u_{M+i}^0 \cos(i\omega t)\right]$$

and similarly for the other five functions. We are going to solve (7)-(12) by collocation. To do that we impose that the functions given in (13)-(18) satisfy the differential equations (7)-(12) at $2M+1$ different times in the interval $[0, T]$. Let these times be $t_j = jT/(2M+1)$, $j = 1, \ldots 2M+1$. Then we have

$$0 = -u^0(t_j) + \sum_{i=1}^{M} \left[i\omega u_i^0 \sin(i\omega t_j) - i\omega u_{M+i}^0 \cos(i\omega t_j)\right]$$

$$+ 0.09 \int_0^{2\pi} F[u^0(t_j) - a^0(t_j) + (u^c(t_j) - a^c(t_j))\cos x + (u^s(t_j) - a^s(t_j))\sin x + h(x)]\ dx \tag{19}$$

$$0 = -u^c(t_j) + \sum_{i=1}^{M} \left[i\omega u_i^c \sin(i\omega t_j) - i\omega u_{M+i}^c \cos(i\omega t_j)\right]$$

$$+ 0.45 \int_0^{2\pi} F[u^0(t_j) - a^0(t_j) + (u^c(t_j) - a^c(t_j))\cos x + (u^s(t_j) - a^s(t_j))\sin x + h(x)]\cos x\ dx \tag{20}$$

$$0 = -u^s(t_j) + \sum_{i=1}^{M} \left[i\omega u_i^s \sin(i\omega t_j) - i\omega u_{M+i}^s \cos(i\omega t_j)\right]$$

$$+ 0.45 \int_0^{2\pi} F[u^0(t_j) - a^0(t_j) + (u^c(t_j) - a^c(t_j))\cos x + (u^s(t_j) - a^s(t_j))\sin x + h(x)]\sin x\ dx \tag{21}$$

$$0 = Bu^0(t_j) - a^0(t_j) + \tau \sum_{i=1}^{M} \left[i\omega a_i^0 \sin(i\omega t_j) - i\omega a_{M+i}^0 \cos(i\omega t_j) \right] \tag{22}$$

$$0 = Bu^c(t_j) - a^c(t_j) + \tau \sum_{i=1}^{M} \left[i\omega a_i^c \sin(i\omega t_j) - i\omega a_{M+i}^c \cos(i\omega t_j) \right] \tag{23}$$

$$0 = Bu^s(t_j) - a^s(t_j) + \tau \sum_{i=1}^{M} \left[i\omega a_i^s \sin(i\omega t_j) - i\omega a_{M+i}^s \cos(i\omega t_j) \right] \tag{24}$$

for $j = 1, \ldots 2M+1$. This gives us $12M+6$ equations: (19)-(24), but there are $12M+7$ unknowns (T being the last unknown). We also have freedom to choose the origin of time, so to remove this degeneracy and obtain the correct number of equations we add one more (largely arbitrary) condition to fix the phase of the periodic orbit: $u^c(0) = 0$, i.e.

$$u_0^c + \sum_{i=1}^{M} u_i^c = 0. \tag{25}$$

Equations (19)-(24) and (25) can be solved straightforwardly using Newton's method, where the integral over x is evaluated using the trapezoidal rule.

We now turn to the representation of the frozen noise, $h(x)$. We assume that it is a uniform random field with mean zero and covariance

$$C(x,y) = \frac{\sigma}{2b} \exp\left[-\frac{\pi}{4} \left(\frac{x-y}{b} \right)^2 \right] \tag{26}$$

so that σ determines its "strength" and b is the characteristic correlation length. We will represent $h(x)$ by its Karhunen-Loève decomposition [23, 20, 34]. To do this we need to find the eigenpairs of C, $\{\lambda_m, e_m(x)\}_{m=1}^{\infty}$, defined by

$$\int_{-\infty}^{\infty} C(x,y) e_m(y)\, dy = \lambda_m e_m(x) \tag{27}$$

and then order the eigenvalues (which are known to be positive and real): $\lambda_1 \geq \lambda_2 \geq \ldots 0$ and normalise the eigenfunctions (which are known to be orthogonal) [34]. The Karhunen-Loève decomposition of h is then

$$h(x) = \sum_{m=1}^{\infty} \sqrt{\lambda_m} e_m(x) \beta_m \tag{28}$$

where the β_m are pairwise independent random variables with mean zero taken from the uniform distribution on $[-1, 1]$. We use a uniform random field rather than the more common Gaussian random field, where the β_m are normally-distributed, because we want the random field $h(x)$ to be bounded. The reason for this is that as the amplitude of $h(x)$ is increased, the moving bump seen in Fig. 1(a) can become "pinned" by the heterogeneity [18, 37]. This type of pinned solution is far in phase space from the original moving bump, and cannot be regarded as a small perturbation from it, due to the nonlinear nature of the problem, so it is not appropriate to consider such a solution. This is also the reason that we will only consider sufficiently small values of σ below. Similar reasoning is used when a random field is constrained by physical reasons to be strictly positive, for example [43].

To find the eigenpairs of C consider the function $\cos(my)$, where $m \in \mathbb{N}^+$. This is periodic on the domain $[0, 2\pi]$ and we have

$$2b\int_0^{2\pi} C(x,y)\cos(my)\,dy = \sigma\int_0^{2\pi}\exp\left[-\frac{\pi}{4}\left(\frac{x-y}{b}\right)^2\right]\cos(my)\,dy \tag{29}$$

$$= \sigma\int_{x-2\pi}^{x}\exp\left[-\frac{\pi}{4}\left(\frac{z}{b}\right)^2\right]\cos(m(x-z))\,dz \tag{30}$$

Now if b is small relative to the domain size (2π), we can approximate this integral by the infinite one:

$$2b\int_0^{2\pi} C(x,y)\cos(my)\,dy \approx \sigma\int_{-\infty}^{\infty}\exp\left[-\frac{\pi}{4}\left(\frac{z}{b}\right)^2\right]\cos(m(x-z))\,dz \tag{31}$$

$$= \sigma\cos(mx)\int_{-\infty}^{\infty}\exp\left[-\frac{\pi}{4}\left(\frac{z}{b}\right)^2\right]\cos(mz)\,dz$$

$$+ \sigma\sin(mx)\int_{-\infty}^{\infty}\exp\left[-\frac{\pi}{4}\left(\frac{z}{b}\right)^2\right]\sin(mz)\,dz \tag{32}$$

$$= 2b\sigma\cos(mx)\exp\left[\frac{-(mb)^2}{\pi}\right] \tag{33}$$

where we have used the fact that [38]

$$\int_{-\infty}^{\infty}\exp\left[-\frac{\pi}{4}\left(\frac{z}{b}\right)^2\right]\cos(mz)\,dz = 2b\exp\left[\frac{-(mb)^2}{\pi}\right] \tag{34}$$

and that $\exp[-(\pi/4)(z/b)^2]\sin(mz)$ is an odd function. Thus (keeping in mind the approximations made above) a partial set of eigenvalues and eigenfunctions for C is

$$\lambda_m^{(1)} = \sigma\exp\left[\frac{-(mb)^2}{\pi}\right]; \qquad e_m^{(1)}(x) = \frac{\cos(mx)}{\sqrt{\pi}} \tag{35}$$

for $m = 1, 2\ldots$. A similar argument shows that the remaining set of eigenvalues and eigenfunctions is

$$\lambda_m^{(2)} = \sigma\exp\left[\frac{-(mb)^2}{\pi}\right]; \qquad e_m^{(2)}(x) = \frac{\sin(mx)}{\sqrt{\pi}} \tag{36}$$

for $m = 1, 2\ldots$. Eigenpairs for other covariance functions can be found either analytically or numerically [34, 23, 20, 43]. We truncate the series (28) to give a finite-dimensional representation of the random field. We write

$$h(x) = \sum_{m=1}^{N}\beta_m\sqrt{\lambda_m^{(1)}}e_m^{(1)}(x) + \sum_{m=1}^{N}\beta_{N+m}\sqrt{\lambda_m^{(2)}}e_m^{(2)}(x) \tag{37}$$

where the $\beta_1, \ldots \beta_{2N}$ are randomly chosen from the uniform distribution on $[-1, 1]$.

The idea is now that for each realisation of the $\{\beta_m\}$ we can numerically solve (19)-(24) and (25). One way to regard the solutions of these equations is that they are given by $12M + 7$ variables, $u_0^0, u_1^0, \ldots, a_{2M}^s, T$, each of which is a function of the $2N$ variables $\beta_1, \ldots, \beta_{2N}$. There are traditionally two different ways to find these functions. The first is stochastic Galerkin [41, 34], where each of the $12M + 7$ variables (for example, T) is expanded in orthogonal polynomials of the $\{\beta_m\}$. This expansion is truncated and then all of the coefficients in this truncated expansion are found by solving a very large set of coupled equations, often exploiting the orthogonality of the polynomials. (The

form of the polynomials is determined by the probability density function of the random variables, the $\{\beta_m\}$. [44, 42]) Once the coefficients have been found, any quantity such as the expected value of, say u_0^0, can be found by integrating over the space of random variables. Unfortunately, modifying code capable of solving (19)-(24) and (25) to find all coefficients in the expansion just mentioned is non-trivial.

The other common alternative is referred to as stochastic collocation [41, 34], which involves solving (19)-(24) and (25) at a number of different points in the random parameter space, i.e. using different $\{\beta_m\}$. We then have the value of all variables $u_0^0, u_1^0, \ldots, a_{2M}^s, T$ at these different points and can use interpolation to estimate the values of these variables at other points in the random parameter space. If the values of $\{\beta_m\}$ at which (19)-(24) and (25) are solved are chosen appropriately, the solutions of these equations at these points can be used to estimate, for example, the expected value of u_0^0 very accurately. This method is referred to as "non-intrusive", as it does not require modification of the code to solve (19)-(24) and (25), just some decisions about the values of $\{\beta_m\}$ to use, and some postprocessing of the results. This method is also trivially parallelisable and is the one we use here.

The main variable we are interested in is $T(\beta_1, \ldots, \beta_{2N})$, the period of the periodic solution, an example of which is shown in Fig. 1. A typical distribution of T, for $10,000$ randomly-chosen $\{\beta_m\}$, is shown in Fig. 2. For these parameter values, the period when $\sigma = 0$ is approximately 124.4007, and the presence of the spatial noise always increases the period. To obtain the expected value of T (which we refer to as $\overline{T}$) we need to average $T(\beta_1, \ldots, \beta_{2N})$ over $\beta_1, \ldots \beta_{2N}$. This average period will itself be a function of parameters of interest such as the strength of the random field, σ, and the correlation length b. Thus, knowing the distribution of the variables $\{\beta_m\}$, we want to calculate the $2N$-dimensional integral

$$\frac{1}{2^{2N}} \int_{-1}^{1} \cdots \int_{-1}^{1} T(\beta_1, \ldots, \beta_{2N}) d\beta_1 \cdots d\beta_{2N} \tag{38}$$

Note that having found $\overline{T}$ it is equally easy to find, for example, the variance of $T(\beta_1, \ldots, \beta_{2N})$:

$$V_T = \frac{1}{2^{2N}} \int_{-1}^{1} \cdots \int_{-1}^{1} \left[T(\beta_1, \ldots, \beta_{2N}) - \overline{T}\right]^2 d\beta_1 \cdots d\beta_{2N} \tag{39}$$

We will evaluate these integrals in several different ways.

The integrals in (19)-(21) are over periodic domains, so the trapeziodal rule which we use converges very quickly as the number of points used increases [40]. We use 275 points in x and assume that this is accurate enough. We also set M, the number of Fourier modes in time, to be $M = 6$, and do not consider varying this number further. We will investigate varying N, which determines the number of modes used to represent the random field $h(x)$, and the number of points used to approximate the integrals in (38). Note that the computational effort to evaluate (38) is proportional to M (and to the number of points used to evaluate the integrals in (19)-(21)) but grows extremely quickly with N, as this is proportional to the dimension of the space to be integrated over.

3. Results

3.1. **Convergence.** We first show some results regarding convergence of three different schemes for evaluating the integral (38). To be concrete we take b (the correlation length of the random field) to be 1. We truncate the series (37) at $N = 3$. Typical realisations

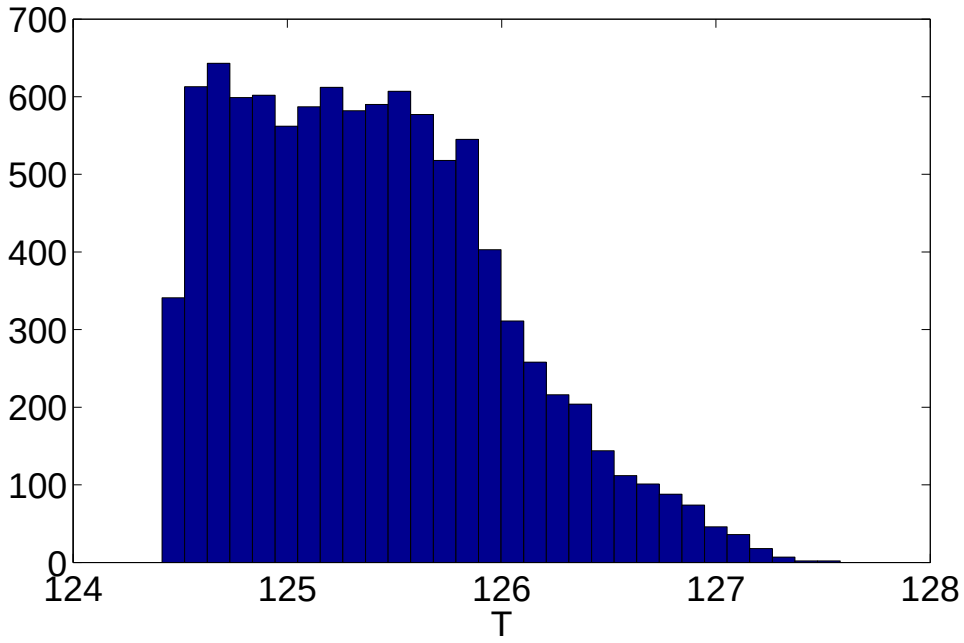

FIGURE 2. A typical distribution of T values, where $10,000$ realisations of the $\beta_1, \ldots \beta_{2N}$ have been used. Parameters: $\sigma = 0.00003, b = 1, N = 3, M = 6, B = 0.1, \tau = 14$.

of the $h(x)$ are shown in Fig. 3 (top) and the average covariance of 1000 realisations is shown in Fig. 3 (bottom). There is significant deviation between the theoretical and actual covariances, and this is mostly due to approximations made in analytically determining the eigenpairs of the covariance operator.

3.1.1. *Monte Carlo.* We wish to approximate the integral in (38). Firstly, consider Monte-Carlo integration. In this method we generate ν vectors K^i, $i = 1, \ldots \nu$, each of length $2N$, where each component of each vector is randomly and independently chosen from a uniform distribution on $[-1, 1]$. We then approximate the $2N$-dimensional integral in (38) by the average

$$\frac{1}{\nu} \sum_{i=1}^{\nu} T(K_1^i, \ldots, K_{2N}^i) \tag{40}$$

This method has the advantage that it is very simple, and will converge to the correct result as $\nu \to \infty$. Unfortunately, it is well-known that the error converges as $1/\sqrt{\nu}$ [17]. The convergence of this method is demonstrated in Fig. 4

3.1.2. *Gaussian quadrature: full grids.* Next we consider using Gaussian quadrature, forming a tensor product of one-dimensional rules [29, 34, 2] in order to approximate the integral in (38). One-dimensional Gauss-Legendre quadrature involves approximating the integral

$$\frac{1}{2} \int_{-1}^{1} f(x) dx \tag{41}$$

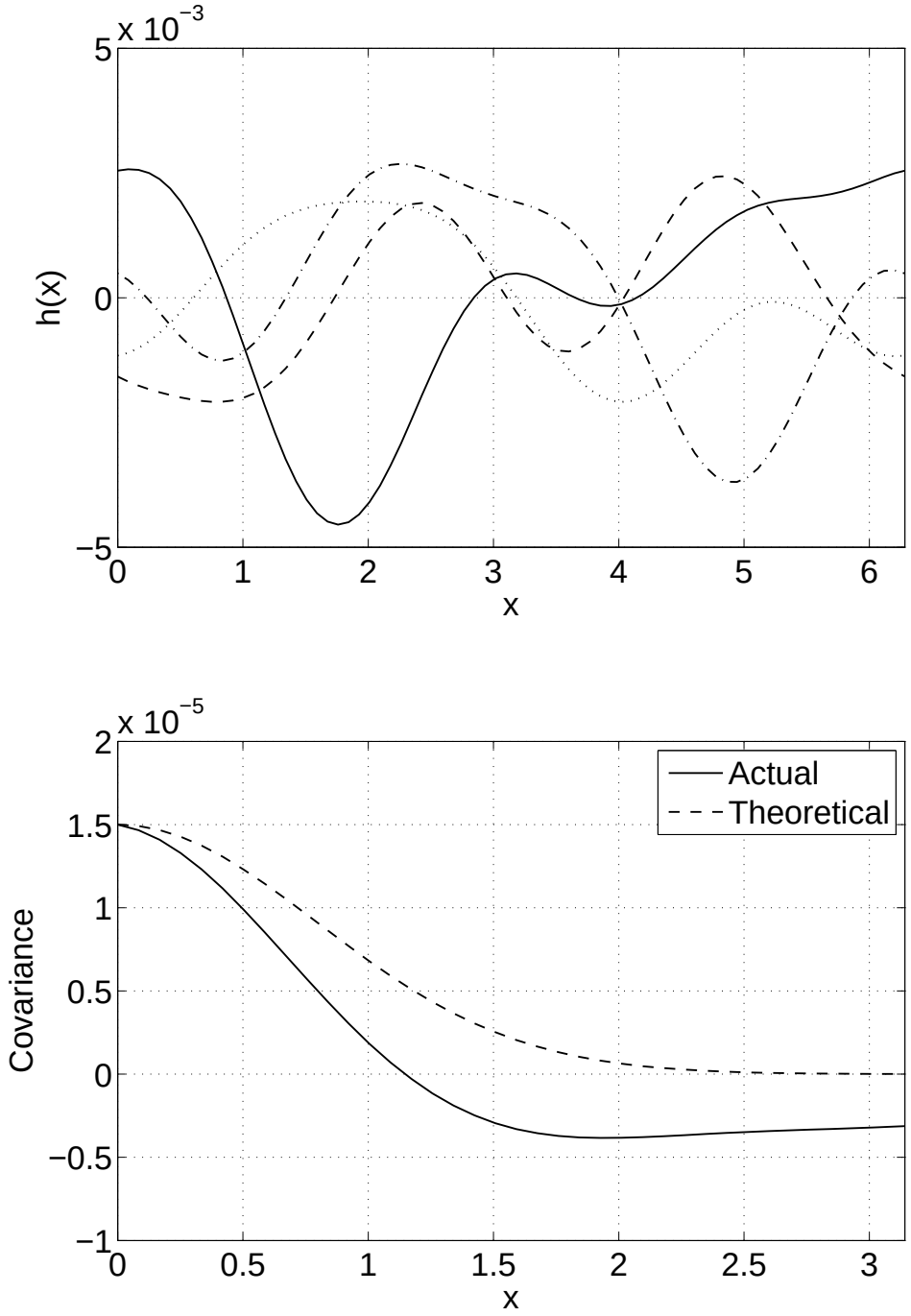

FIGURE 3. Top: four typical realisations of $h(x)$ for $b = 1$, given by (37). Bottom: theoretical covariance of $h(x)$, given by (26) (dashed), and the average covariance of 1000 independent realisations (solid). Parameters: $\sigma = 0.00003, b = 1, N = 3$.

for sufficiently smooth functions f by the sum

$$\sum_{j=1}^{\widehat{N}} w_j f(x_j) \tag{42}$$

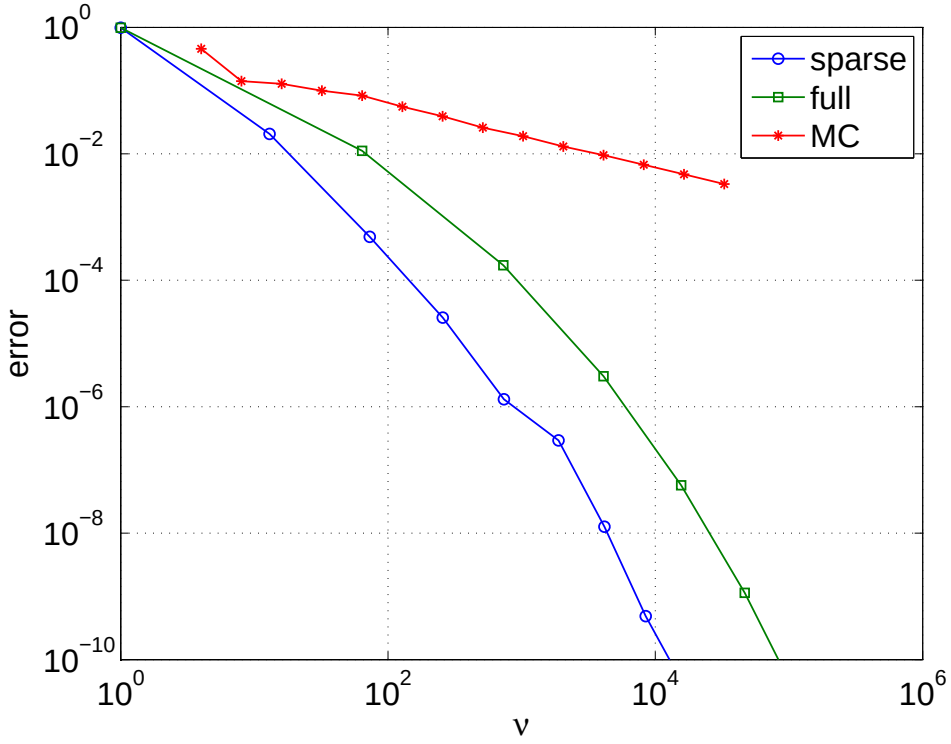

FIGURE 4. Error convergence. MC: Monte-Carlo integration. For large ν the data points lie on a line with slope $-1/2$, as expected. full: full tensor product. sparse: sparse tensor product. ν is the number of $2N$-dimensional vectors needed in the approximation of the integral in (38), i.e. the total number of distinct values of $T(\beta_1, \ldots, \beta_{2N})$ that are used to approximate (38). Parameters: $\sigma = 0.00003, b = 1, N = 3, M = 6, B = 0.1, \tau = 14$.

where x_j is the jth root of $P_{\widehat{N}}$, the $\widehat{N}$th Legendre polynomial (normalised so that $P_{\widehat{N}}(1) = 1$), and the weights w_j are given by

$$w_j = \frac{1}{(1 - x_j^2)\left[P'_{\widehat{N}}(x_j)\right]^2} \tag{43}$$

These rules can be used to approximate multi-dimensional integrals where the variable in each direction is uniformly distributed, in the obvious way. Figure 5 shows the tensor product in two spatial dimensions, and weights, for $\widehat{N} = 10$.

For fixed $\widehat{N}$ we approximate the integral (38) by the multiple sum

$$\sum_{j_1=1}^{\widehat{N}} \sum_{j_2=1}^{\widehat{N}} \cdots \sum_{j_{2N}=1}^{\widehat{N}} w_{j_1} w_{j_2} \ldots w_{j_{2N}} T(x_{j_1}, \ldots, x_{j_{2N}}) \tag{44}$$

There are a total of $(\widehat{N})^{2N}$ terms in this multiple sum, which grows rapidly as a function of $\widehat{N}$ for moderate to large N — this is the curse of dimensionality. Results using this method are shown in Fig. 4, where $\nu = (\widehat{N})^{2N}$. We see rapid convergence, as expected from a spectral method such as this [40]. However, the curse of dimensionality makes

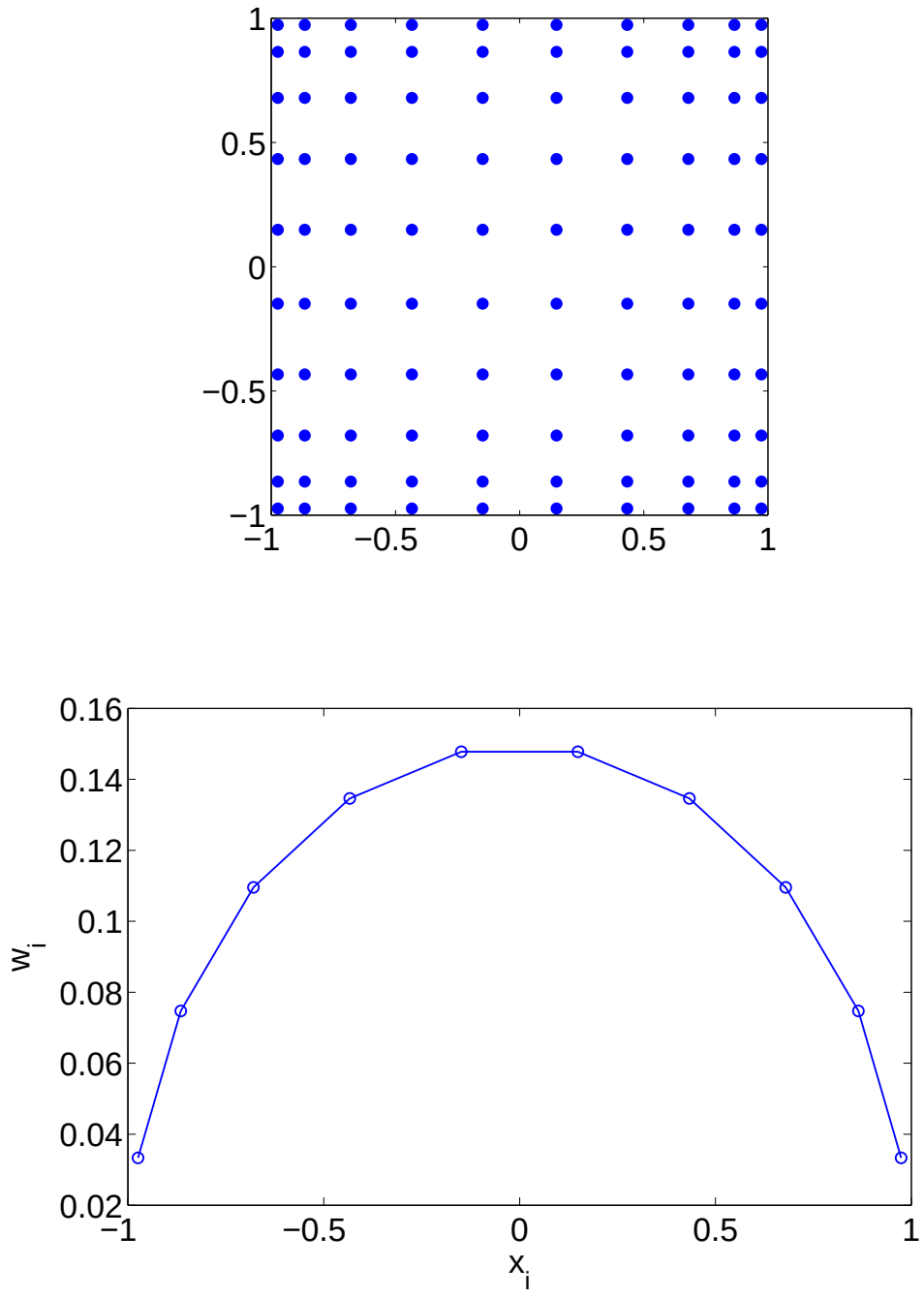

FIGURE 5. Top: tensor product in two dimensions, formed from two one-dimensional Gauss-Legendre rules. Bottom: weights w_i as a function of the nodes x_i, for $\widehat{N} = 10$.

this method infeasible for many problems. For example, if $N = 5$ and $\widehat{N} = 5$, i.e. we use just five points in each of 10 random dimensions, we have $\nu \approx 10^7$.

3.1.3. *Gaussian quadrature: sparse grids.* The third method we consider involves the use of sparse tensor grids [29, 22, 19, 3]. Tensor products are still formed, as in Fig. 5, but many of the points are then discarded, as they do not contribute significantly to the evaluation of the integral. For a specific spatial dimension, different "levels" of grids,

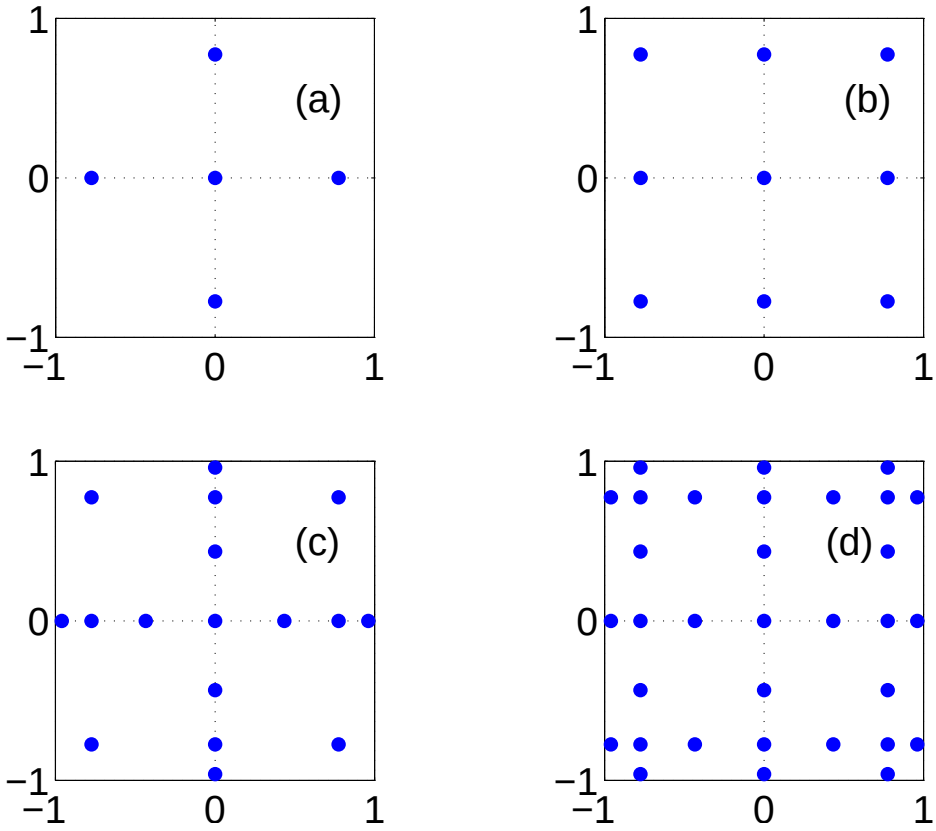

FIGURE 6. Sparse tensor products in two spatial dimensions for (a)–(d): levels 2–5. The number of points is, respectively, $5, 9, 17$ and 33.

and thus accuracies, are constructed. An example is shown in Fig. 6 for two spatial dimensions. (We use the code associated with [22], available at http://www.sparse-grids.de/) We do not present the general theory here but instead refer the reader to references above. For a given level of accuracy, sparse grids use fewer points than full tensor grids, and the advantage of using sparse grids as opposed to full increases as the dimension of the space to be integrated over increases. Figure 4 shows results from using sparse grids. We see that this method is the most accurate of the three considered, converging more rapidly than the full tensor product. We expect this advantage to increase as N, the number of dimensions integrated over, increases.

3.2. **Varying parameters.** Having compared three common schemes for approximating the integral (38), we now use the most accurate one (sparse tensor products) to investigate the effects of varying parameters in the model. We first consider varying the "strength" of the random field, σ. To obtain specific results we keep the correlation length b at $b = 1$ and set $N = 6$. We set the sparse grid level to be 5, which means using a total of $11,073$ points in the approximation of (38). The results are shown in Fig. 7, and we see that both the mean and standard deviation of the distribution of periods increases almost linearly with σ.

In Fig. 8 we vary the correlation length b. Because the coefficients of the random field $h(x)$ decay more slowly as b is decreased, we need to keep a large number of terms in the truncation (37) to accurately represent the field $h(x)$, i.e. we need to integrate over a high dimensional space. We set $N = 50$, which, for the level we choose, gives $20,001$

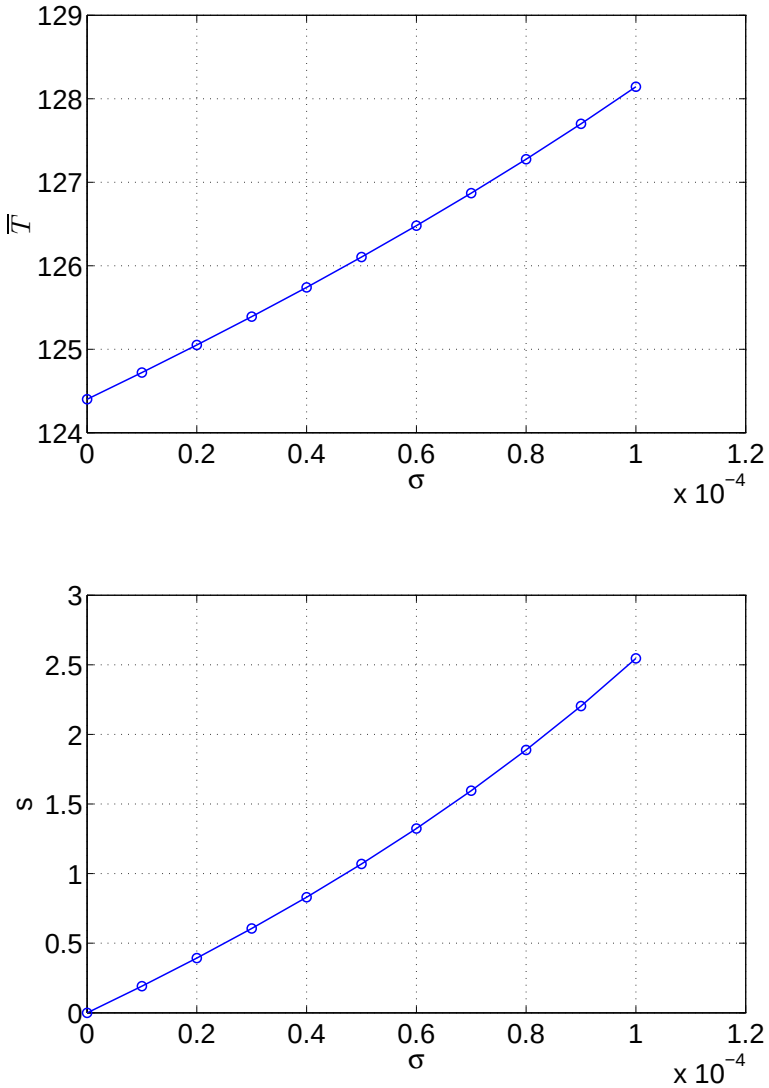

FIGURE 7. Mean period, $\overline{T}$ (top) and standard deviation, ($s \equiv \sqrt{V_T}$) (bottom) as a function of random field strength σ. Parameters: $b = 1, N = 6$.

points in the approximation of (38). We see that for these parameter values and the truncations used, the standard deviation of the distribution of periods decreases as b is increased, while the mean period shows a non-monotonic dependence on b.

Note that for this type of high-dimensional integration, full tensor grids are impossible to use. Even using sparse tensor grids, as above, is problematic, as the number of points used still grows very rapidly with the level used, and a large amount of time is spent actually calculating the grid points before they are used. However Monte Carlo methods are still feasible, as are other extensions of Monte Carlo methods such as Quasi-Monte Carlo (QMC) [21, 12, 27, 17]. QMC methods are similar to Monte Carlo in that the integrand is evaluated at many points and then averaged, but in QMC methods the points are not randomly chosen, but rather chosen in some "optimal" way. Many variations exist, and rather than go into details here we show in Fig. 9 a comparison between Monte Carlo and one particular QMC algorithm. We see that QMC does better than Monte Carlo, at least for these parameter values. The convergence rate for the error

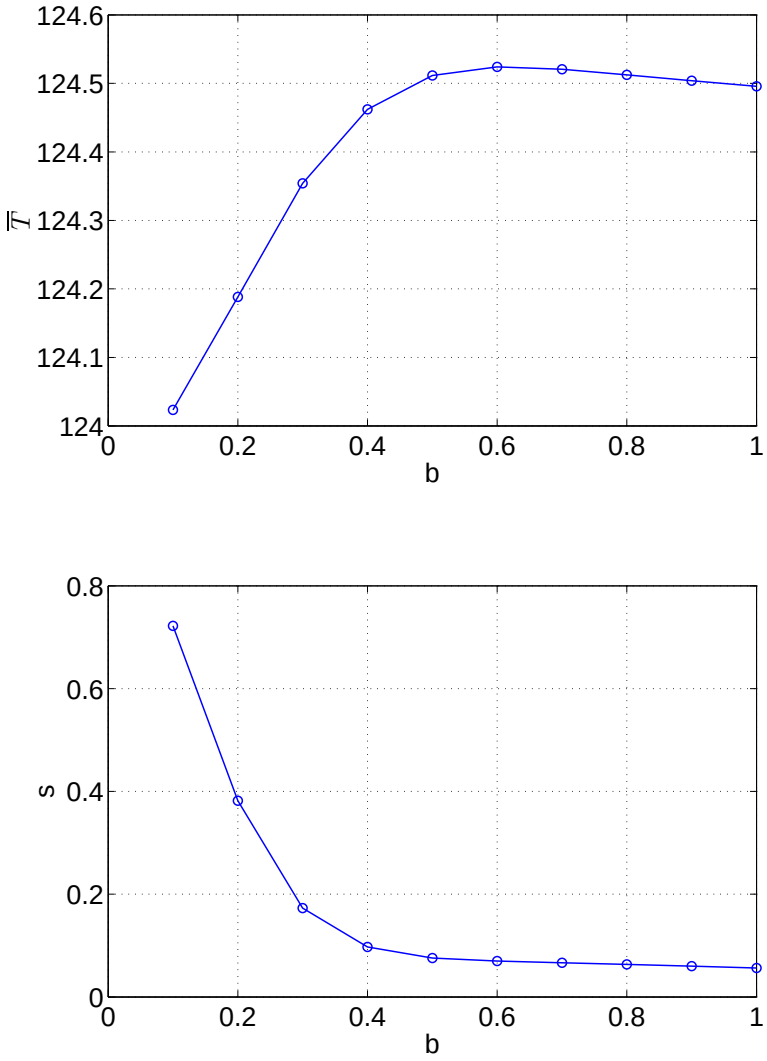

FIGURE 8. Mean period, $\overline{T}$ (top) and standard deviation, V_T (bottom) as a function of random field correlation length b. Parameters: $\sigma = 3 \times 10^{-6}, N = 50$.

in the Monte Carlo method is known to scale as $1/\sqrt{\nu}$, and "randomised" QMC methods can be used to obtain error estimates for these types of method [21].

Figure 10 shows the same calculation as in the top panel of Fig. 8, but with QMC. The results are essentially identical, and if errorbars were plotted in Fig. 10 they would be smaller than the markers shown.

4. Other forms of heterogeneity

In the model (1)-(2) we included the random field inside the nonlinear function F, thinking of it as a spatial perturbation of the firing threshold. We now show how several other forms of heterogeneity could be dealt with using the ideas presented here.

4.1. **Modulated connectivity.**

Suppose that (1) was replaced by

$$\frac{\partial u(x,t)}{\partial t} = -u(x,t) + \int_0^{2\pi} G(x-y)[1+h(y)]F[u(y,t)-a(y,t)]dy \tag{45}$$

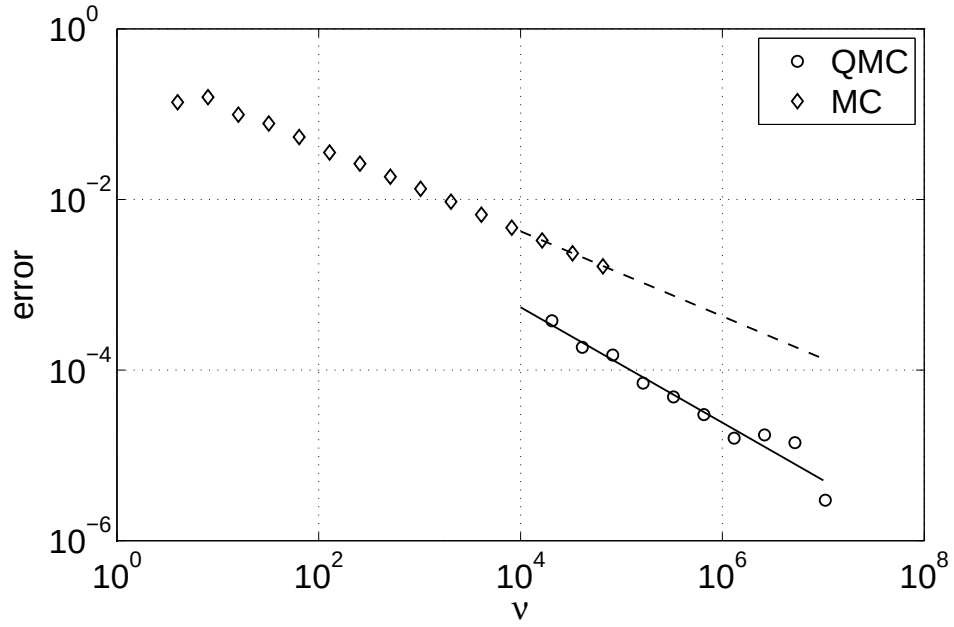

FIGURE 9. Error in calculating the mean period as a function of the number of integrand evaluations for Monte Carlo and Quasi-Monte Carlo methods (rule `lattice-38005-1024-1048576.5000` from `http://web.maths.unsw.edu.au/~fkuo/lattice/index.html`). The dashed line has slope -0.50 and the solid has slope -0.68. Parameters: $b = 0.1, \sigma = 10^{-6}, N = 50$.

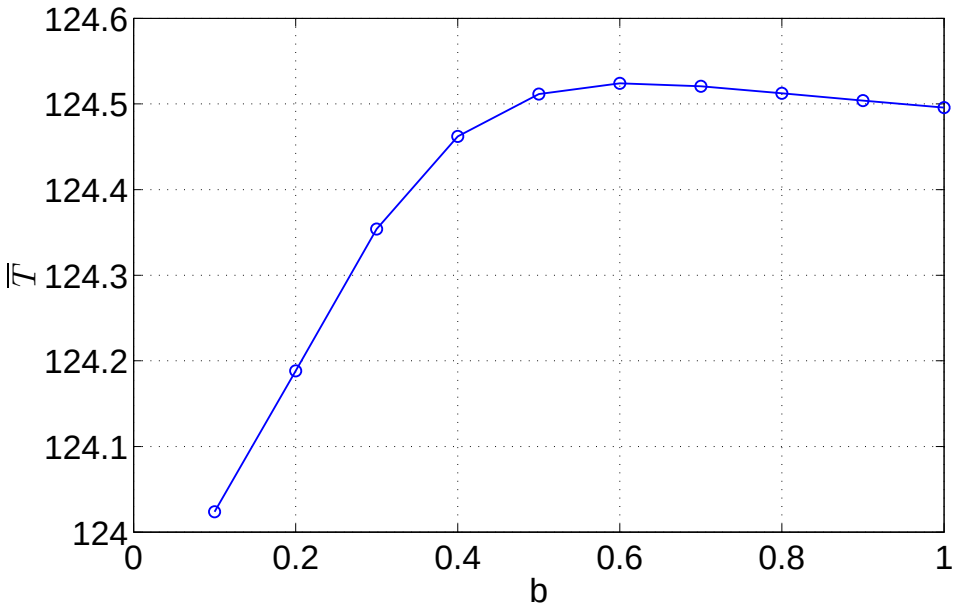

FIGURE 10. Mean period, $\overline{T}$ as a function of random field correlation length b, calculated using the same QMC algorithm as in Fig. 9. Errorbars are smaller than the markers shown. Parameters: $\sigma = 3 \times 10^{-6}, N = 50$.

as in [14, 7], where we can think of the new connectivity, $G(x-y)[1+h(y)]$, as no longer being a function of $x-y$ only. The above analysis would go through, with (10)-(12) being the same, but (7)-(9) being replaced by

(46)
$$\frac{du^0}{dt} = -u^0 + 0.09\int_0^{2\pi}[1+h(x)]F[u^0 - a^0 + (u^c - a^c)\cos x + (u^s - a^s)\sin x]\ dx$$

(47)
$$\frac{du^c}{dt} = -u^c + 0.45\int_0^{2\pi}[1+h(x)]F[u^0 - a^0 + (u^c - a^c)\cos x + (u^s - a^s)\sin x]\cos x\ dx$$

(48)
$$\frac{du^s}{dt} = -u^s + 0.45\int_0^{2\pi}[1+h(x)]F[u^0 - a^0 + (u^c - a^c)\cos x + (u^s - a^s)\sin x]\sin x\ dx$$

respectively, with a corresponding modification of (19)-(21). Parametrising $h(x)$ as in (37) we can find $T(\beta_1, \ldots, \beta_{2N})$ by solving this new set of equations as before, and this form of heterogeneity introduces no new complexity. Results are shown in Fig. 11. We see that as above, both the mean period and its standard deviation increase as σ is increased.

4.2. **Modulated Drive.** Suppose instead that (1) was replaced by

$$\frac{\partial u(x,t)}{\partial t} = -u(x,t) + \int_0^{2\pi} G(x-y)F[u(y,t) - a(y,t)]dy + h(x) \tag{49}$$

as originally proposed by Amari [1]. Using $h(x)$ as in (37) and writing

$$u(x,t) = U^0(t) + \sum_{i=1}^{\infty}[U_i^c(t)\cos(ix) + U_i^s(t)\sin(ix)] \tag{50}$$

and

$$a(x,t) = A^0(t) + \sum_{i=1}^{\infty}[A_i^c(t)\cos(ix) + A_i^s(t)\sin(ix)] \tag{51}$$

we see that all $U_i^c(t), U_i^s(t), A_i^c(t)$ and $A_i^s(t)$ will decay to zero if $i > N$, so we can truncate (50) and (51) at $i = N$. For $2 \le i \le N$ we have (after transients)

$$0 = -U_i^c + \beta_i\sqrt{\frac{\lambda_i^{(1)}}{\pi}} \qquad \text{and} \qquad 0 = -U_i^s + \beta_{N+i}\sqrt{\frac{\lambda_i^{(2)}}{\pi}} \tag{52}$$

and

$$0 = BU_i^c - A_i^c \qquad \text{and} \qquad 0 = BU_i^s - A_i^s \tag{53}$$

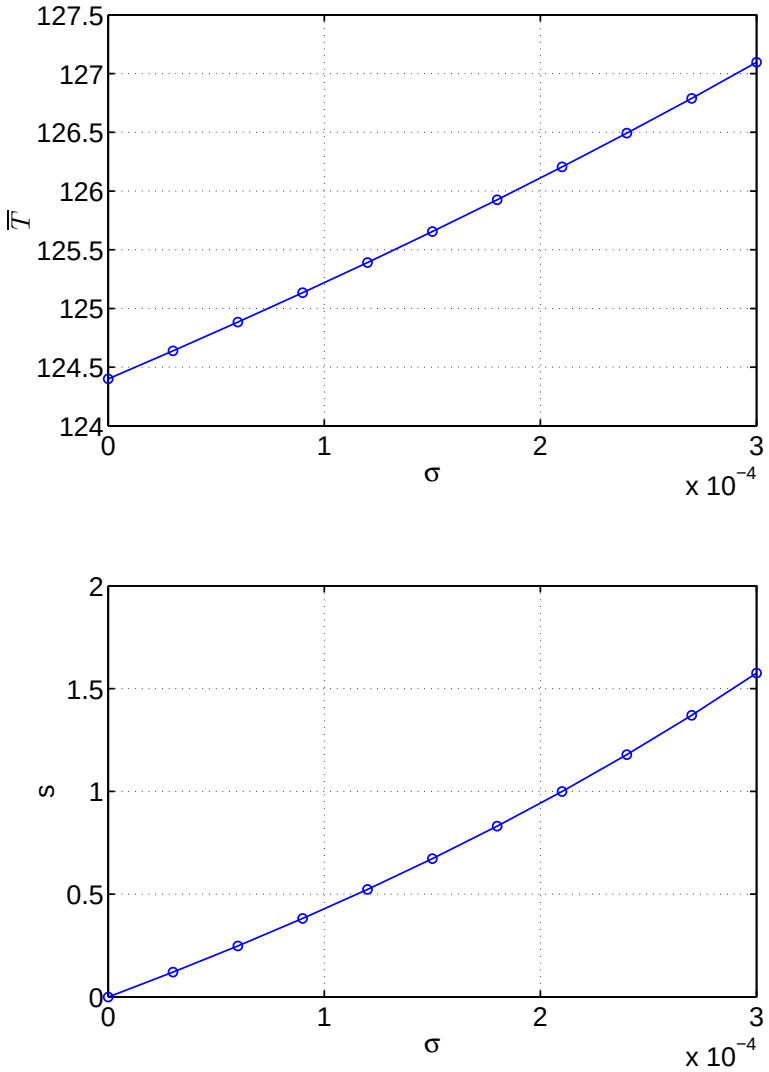

FIGURE 11. Modulated connectivity. Mean period, $\overline{T}$ (top) and standard deviation, $s = \sqrt{V_T}$ (bottom) as a function of random field strength σ. Parameters: $b = 1, N = 6$.

which can all be trivially solved. Now $U^0, U_1^c, U_1^s, A^0, A_1^c$ and A_1^s satisfy

$$\frac{dU^0}{dt} = -U^0 + 0.09 \int_0^{2\pi} F[u(x,t) - a(x,t)]\, dx \tag{54}$$

$$\frac{dU_1^c}{dt} = -U_1^c + 0.45 \int_0^{2\pi} F[u(x,t) - a(x,t)] \cos x\, dx + \beta_1 \sqrt{\frac{\lambda_1^{(1)}}{\pi}} \tag{55}$$

$$\frac{dU_1^s}{dt} = -U_1^s + 0.45 \int_0^{2\pi} F[u(x,t) - a(x,t)] \sin x\, dx + \beta_{N+1} \sqrt{\frac{\lambda_1^{(2)}}{\pi}} \tag{56}$$

$$\tau \frac{dA^0}{dt} = BU^0 - A^0 \tag{57}$$

$$\tau \frac{dA_1^c}{dt} = BU_1^c - A_1^c \tag{58}$$

$$\tau \frac{dA_1^s}{dt} = BU_1^s - A_1^s \tag{59}$$

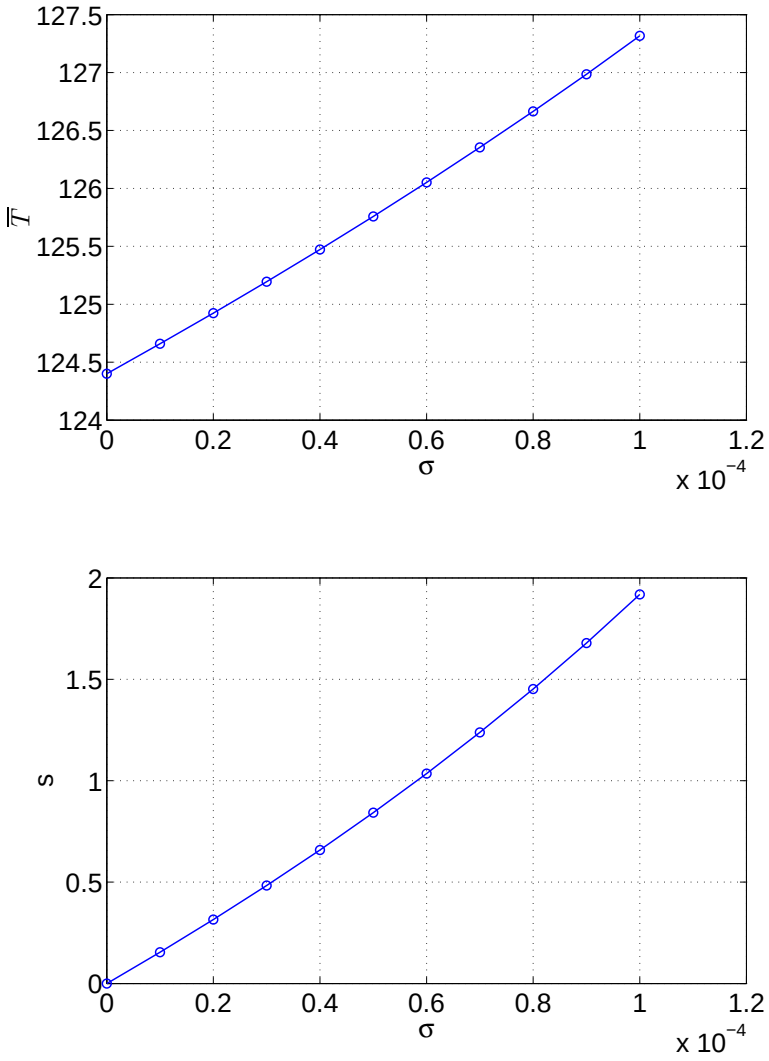

FIGURE 12. Modulated Drive. Mean period, $\overline{T}$ (top) and standard deviation, $s = \sqrt{V_T}$ (bottom) as a function of random field strength σ. Parameters: $b = 1, N = 6$.

This set of equations is no more complex than (7)-(12) and can be solved the same way. The results of varying the random field strength σ are shown in Fig. 12. Comparing with Fig. 7 and 11 we see qualitatively the same behaviour: increasing the heterogeneity both slows the bump and increases the width of the distribution of periods.

5. Conclusion

In this chapter we have used ideas from the field of Uncertainty Quantification to investigate the effects of spatial heterogeneity on the speed of a moving "bump" of activity in a neural field model. Neural field models are intrinsically infinite-dimensional, as is the spatially-extended "frozen noise" that we included in the model. In order to make computational progress we need to represent these processes in a finite-dimensional way. The form of the coupling function G (constant plus cosine) allowed us to exactly write the neural field dynamics (after transients) in the form of six coupled ODEs (7)-(12), thus making the spatial part of the dynamics finite-dimensional. Any other spatially-periodic

coupling function could be represented arbitrarily well by a finite number of similar spatial modes via a Fourier series, resulting in a similar set of ODEs. These ODEs can be approximately solved in any number of ways, but collocation, as used here, is very efficient. It should be emphasised that the type of solution we were interested in, namely a moving bump, meant that we were interested in periodic solutions of these ODEs. If we were interested in, for example, a moving front [11, 5], we would look for different sorts of solutions. A specific example of such a front moving over a heterogeneous domain is given in Sec. 4.1 of [15]. And as is standard, the noise process is approximated in a finite-dimensional way by truncating the Karhunen-Loève decomposition (28).

Finding the expected value of a quantity (in this case, the period of a periodic orbit) in a system with stochastic or uncertain parameters is equivalent to averaging over a multi-dimensional space. For a small to moderate dimensions such an integral can be performed using full or sparse tensor product grids [29], but for high-dimensional integrals techniques such as Quasi-Monte Carlo [17] must be used. We have demonstrated each of these methods and found several interesting results. For the parameters studied, adding spatial noise to the system always slows the moving bump. Also, varying the spatial scale of the noise shows a nonmonotonic response of the bump's speed (Figs. 8 and 10).

The results presented here are computationally intensive, and the field of uncertainty quantification can only benefit from both continuing increases in computational power and continued theoretical advances.

Conflict of interest: The author declares that they have no conflict of interest.

References

[1] S. Amari. Dynamics of pattern formation in lateral-inhibition type neural fields. *Biological cybernetics*, 27(2):77–87, 1977.

[2] Ivo Babuška, Fabio Nobile, and Raúl Tempone. A stochastic collocation method for elliptic partial differential equations with random input data. *SIAM review*, 52(2):317–355, 2010.

[3] V. Barthelmann, E. Novak, and K. Ritter. High dimensional polynomial interpolation on sparse grids. *Advances in Computational Mathematics*, 12(4):273–288, 2000.

[4] R Ben-Yishai, R L Bar-Or, and H Sompolinsky. Theory of orientation tuning in visual cortex. *Proceedings of the National Academy of Sciences*, 92(9):3844–3848, 1995.

[5] CA Brackley and MS Turner. Random fluctuations of the firing rate function in a continuum neural field model. *Physical Review E*, 75(4):041913, 2007.

[6] Paul C Bressloff and Jeremy Wilkerson. Traveling pulses in a stochastic neural field model of direction selectivity. *Frontiers in Computational Neuroscience*, 6(90), 2012.

[7] P.C. Bressloff. Traveling fronts and wave propagation failure in an inhomogeneous neural network. *Physica D: Nonlinear Phenomena*, 155(1):83–100, 2001.

[8] P.C. Bressloff. From invasion to extinction in heterogeneous neural fields. *Journal of mathematical neuroscience*, 2:6, 2012.

[9] P.C. Bressloff. Spatiotemporal dynamics of continuum neural fields. *Journal of Physics A: Mathematical and Theoretical*, 45(3):033001, 2012.

[10] P.C. Bressloff and S.E. Folias. Front bifurcations in an excitatory neural network. *SIAM Journal on Applied Mathematics*, 65(1):131–151, 2004.

[11] P.C. Bressloff and M.A. Webber. Front propagation in stochastic neural fields. *SIAM Journal on Applied Dynamical Systems*, 11(2):708–740, 2012.

[12] Ronald Cools, Frances Y Kuo, and Dirk Nuyens. Constructing embedded lattice rules for multivariate integration. *SIAM Journal on Scientific Computing*, 28(6):2162–2188, 2006.

[13] S. Coombes. Waves, bumps, and patterns in neural field theories. *Biological Cybernetics*, 93(2):91–108, 2005.

[14] S. Coombes and CR Laing. Pulsating fronts in periodically modulated neural field models. *Physical Review E*, 83(1):011912, 2011.

[15] S. Coombes, H. Schmidt, CR Laing, N. Svanstedt, and JA Wyller. Waves in random neural media. *Discrete Continuous Dyn. Syst*, 2012.

[16] S. Coombes, N.A. Venkov, L. Shiau, I. Bojak, D.T.J. Liley, and C.R. Laing. Modeling electrocortical activity through improved local approximations of integral neural field equations. *Physical Review E*, 76(5):051901, 2007.

[17] Josef Dick, Frances Y. Kuo, and Ian H. Sloan. High-dimensional integration: The quasi-Monte Carlo way. *Acta Numerica*, 22:133–288, 5 2013.

[18] Stefanos E Folias. Nonlinear analysis of breathing pulses in a synaptically coupled neural network. *SIAM Journal on Applied Dynamical Systems*, 10(2):744–787, 2011.

[19] T. Gerstner and M. Griebel. Numerical integration using sparse grids. *Numerical algorithms*, 18(3):209–232, 1998.

[20] Roger Ghanem and Pol D Spanos. *Stochastic finite elements: a spectral approach*. Springer-Verlag, 1991.

[21] Mike Giles, Frances Y Kuo, Ian H Sloan, and Benjamin J Waterhouse. Quasi-Monte Carlo for finance applications. *ANZIAM Journal*, 50:C308–C323, 2008.

[22] F. Heiss and V. Winschel. Likelihood approximation by numerical integration on sparse grids. *Journal of Econometrics*, 144(1):62–80, 2008.

[23] SP Huang, ST Quek, and KK Phoon. Convergence study of the truncated Karhunen–Loeve expansion for simulation of stochastic processes. *International journal for numerical methods in engineering*, 52(9):1029–1043, 2001.

[24] Zachary P Kilpatrick and Bard Ermentrout. Wandering bumps in stochastic neural fields. *SIAM Journal on Applied Dynamical Systems*, 12(1):61–94, 2013.

[25] Z.P. Kilpatrick, S.E. Folias, and P.C. Bressloff. Traveling pulses and wave propagation failure in inhomogeneous neural media. *SIAM Journal on Applied Dynamical Systems*, 7(1):161–185, 2008.

[26] Christian Kuehn and Martin Riedler. Large deviations for nonlocal stochastic neural fields. *The Journal of Mathematical Neuroscience*, 4(1):1, 2014.

[27] Frances Y Kuo and Ian H Sloan. Lifting the curse of dimensionality. *Notices of the AMS*, 52(11):1320–1328, 2005.

[28] C. Laing and S. Coombes. The importance of different timings of excitatory and inhibitory pathways in neural field models. *Network: Computation in Neural Systems*, 17(2):151–172, 2006.

[29] Carlo Laing, Yu Zou, Ben Smith, and Ioannis Kevrekidis. Managing heterogeneity in the study of neural oscillator dynamics. *The Journal of Mathematical Neuroscience*, 2(1):5, 2012.

[30] CR Laing, TA Frewen, and IG Kevrekidis. Coarse-grained dynamics of an activity bump in a neural field model. *Nonlinearity*, 20(9):2127, 2007.

[31] C.R. Laing and A. Longtin. Noise-induced stabilization of bumps in systems with long-range spatial coupling. *Physica D: Nonlinear Phenomena*, 160(3):149–172, 2001.

[32] C.R. Laing and W.C. Troy. PDE methods for nonlocal models. *SIAM J. Appl. Dyn. Syst*, 2(3):487–516, 2003.

[33] C.R. Laing, W.C. Troy, B. Gutkin, and G.B. Ermentrout. Multiple bumps in a neuronal model of working memory. *SIAM Journal on Applied Mathematics*, 63:62, 2002.

[34] OP Le Maître and O.M. Knio. *Spectral methods for uncertainty quantification*. Springer, 2010.

[35] MR Owen, CR Laing, and S. Coombes. Bumps and rings in a two-dimensional neural field: splitting and rotational instabilities. *New Journal of Physics*, 9:378, 2007.

[36] D.J. Pinto and G.B. Ermentrout. Spatially structured activity in synaptically coupled neuronal networks: I. traveling fronts and pulses. *SIAM journal on Applied Mathematics*, 62(1):206–225, 2001.

[37] J. Rankin, A.I. Meso, G.S. Masson, O. Faugeras, and P. Kornprobst. Bifurcation study of a neural field competition model with an application to perceptual switching in motion integration. *Journal of Computational Neuroscience*, 36(2):193–213, 2014.

[38] Tony Shardlow. Numerical simulation of stochastic PDEs for excitable media. *Journal of Computational and Applied Mathematics*, 175(2):429 – 446, 2005.

[39] Moira L. Steyn-Ross, D. A. Steyn-Ross, J. W. Sleigh, and D. R. Whiting. Theoretical predictions for spatial covariance of the electroencephalographic signal during the anesthetic-induced phase

transition: Increased correlation length and emergence of spatial self-organization. *Phys. Rev. E*, 68:021902, Aug 2003.

[40] L.N. Trefethen. *Spectral methods in MATLAB*, volume 10. Society for Industrial Mathematics, 2000.

[41] Dongbin Xiu. Fast numerical methods for stochastic computations: a review. *Communications in computational physics*, 5(2-4):242–272, 2009.

[42] Dongbin Xiu. *Numerical methods for stochastic computations: a spectral method approach*. Princeton University Press, 2010.

[43] Dongbin Xiu and Jan S Hesthaven. High-order collocation methods for differential equations with random inputs. *SIAM Journal on Scientific Computing*, 27(3):1118–1139, 2005.

[44] Dongbin Xiu and George Em Karniadakis. The Wiener–Askey polynomial chaos for stochastic differential equations. *SIAM Journal on Scientific Computing*, 24(2):619–644, 2002.

[45] Dongbin Xiu, Ioannis G Kevrekidis, and Roger Ghanem. An equation-free, multiscale approach to uncertainty quantification. *Computing in science & engineering*, 7(3):16–23, 2005.

Institute of Natural and Mathematical Sciences, Massey University, Private Bag 102-904 NSMC, Auckland, New Zealand

E-mail address: c.r.laing@massey.ac.nz